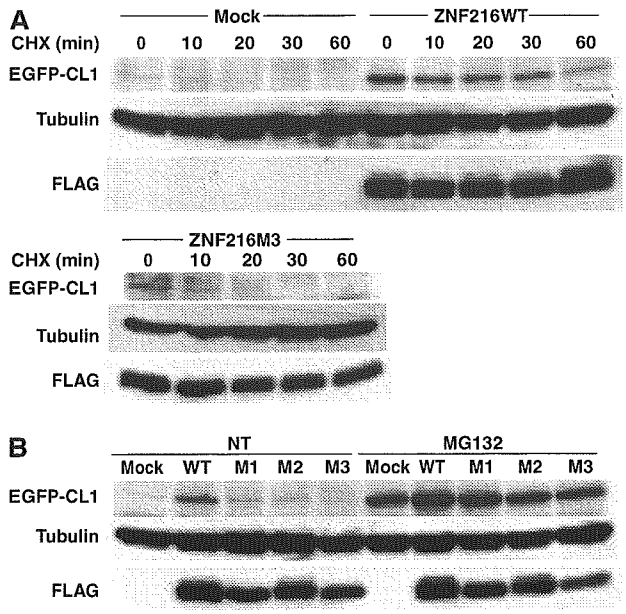

Figure 8 Ectopic expression of ZNF216-affected protein degradation. (**A**) Degradation of EGFP-CL1 protein was delayed by overexpression of ZNF216. 293 cells stably expressing EGFP-CL1 were transfected with plasmid of ZNF216WT, ZNF216M3 or pcDNA3 (mock). Estimated half-lives of the EGFP-CL1 are 35, 11 and 11 min in ZNF216WT-, ZNF216M3- and mock-transfected cells, respectively. *De novo* protein synthesis was arrested by cycloheximide (CHX). The membrane was re-probed with tubulin antibody to control for protein loading (tubulin) and FLAG antibody to detect ZNF216 expression (FLAG). (**B**) Degradation of EGFP-CL1 protein in the presence of various ZNF216 constructs. HEK293 cells stably expressing EGFP-CL1 were transfected with plasmids expressing the indicated mutants. Transfected cells were not treated (NT) or MG132-treated (MG132), and EGFP-CL1 protein was detected with an anti-GFP antibody (EGFP-CL1). The membrane was re-probed with tubulin antibody to control for protein loading (tubulin) and FLAG antibody to detect ZNF216 expression (FLAG).

shown that TNFα induces catabolic conditions through UPS during cancer cachexia (Mitch and Price, 2001). Recently, it has been reported that mice deficient in molecules involved in the NF-κB pathway exhibit resistance to muscular atrophy (Cai *et al*, 2004; Hunter and Kandarian, 2004; McKinnell and Rudnicki, 2004). On the other hand, the IGF-FOXO axis has been suggested to regulate muscle mass through induction of 'atrogenes' such as Murf1 and MAFbx/Atrogin-1 (Sandri *et al*, 2004; Stitt *et al*, 2004). Although we provide evidence that *Znf216* is downstream of FOXO, the NF-κB pathway could represent an alternative signal inducing ZNF216. Indeed, we have identified *Znf216* as a gene induced by RANKL, a TNF family ligand (Hishiya *et al*, 2005) which activates the NF-κB pathway through RANK (Anderson *et al*, 1997; Lacey *et al*, 1998). Moreover, TNFα and IL-1β upregulate expression of ZNF216 in fibroblasts and macrophages (Hishiya *et al*, 2005). These results suggest that *Znf216* may be activated by NF-κB. Huang *et al* (2004) recently reported that ZNF216 inhibits the NF-κB pathway. Whereas treatment with TNFα or overexpression of TRAF6 dramatically activated a reporter driven by NF-κB response elements, ectopic expression of A20/TNFAIP3 but not ZNF216 inhibited NF-κB activation (not shown). Using mouse embryonic fibroblasts, splenocytes or bone marrow cells from $Znf216^{lex/lex}$ or wild-type mice, no significant differences were observed in TNFα-dependent NF-κB activation, LPS-induced cytokine expression or proliferation (unpublished data). Therefore, ZNF216 seems to function as a downstream effector (i.e., a component of the UPS) rather than a specific negative regulator of NF-κB signaling, although ZNF216 function in that pathway is still under investigation. Whereas expression of ZNF216 is not restricted to muscle, such expression was induced upon muscular atrophy and loss of function of *Znf216* promotes resistance to denervation-induced atrophy, thereby suggesting that it fulfills the definition of an 'atrogene'.

As it is in skeletal muscle, ZNF216 is highly expressed in the brain (Scott *et al*, 1998). Aberrations in the UPS have been documented in the pathogenesis of neurodegenerative diseases such as Parkinson's and Huntington's diseases (Ross and Poirier, 2004). Massive accumulation of ubiquitinylated proteins, which are often aggregated and impair the UPS leading to neuronal degeneration, has been observed in these pathogenic conditions (Ciechanover and Brundin, 2003; Korhonen and Lindholm, 2004). In cultured cells, blocking the UPS by proteasome inhibitors leads to accumulation of ubiquitinylated proteins. These ubiquitinylated proteins are then transferred to perinuclear locations and form aggresomes (Johnston *et al*, 1998). As shown here, ZNF216 is localized in aggresomes together with ubiquitinylated proteins. Interestingly, proteomic analysis of a protein complex containing HDAC6, a protein often associated with aggresomes (Kawaguchi *et al*, 2003), showed that the complex included AWP1, a structural homologue of ZNF216 (Seigneurin-Berny *et al*, 2001). Although it is unclear whether ZNF216 is involved in aggresome formation, there is great interest in the role of ZNF216 in the pathogenesis of neurodegenerative diseases.

Molecular function of an A20-containing protein, ZNF216

In muscle atrophy, more ubiquitinylated proteins accumulate in muscle from $Znf216^{lex/lex}$ mice than in muscle from wild-type mice, suggesting an abnormal UPS function. Inhibition of neither polyubiquitinylation nor DUB activity was observed in ZNF216. Although our *in vivo* data showed significant accumulation of polyubiquitinylated proteins in muscle from $Znf216^{lex/lex}$ mice, there is a possibility that ZNF216 is a ubiquitin-ligase. It has been recently reported that A20/TNFAIP3 protein possesses ubiquitin ligase activity against RIP through its ZnF-A20 repeats (Wertz *et al*, 2004). We asked whether the ZnF-A20 of ZNF216 exhibited activity similar to A20/TNFAIP3, but *in vitro* ubiquitinylation assays were negative (Supplementary Figure S6). In fact, the ZnF-A20 of A20/TNFAIP3 protein does not bind polyubiquitin chains as does the ZnF-A20 of ZNF216 (Supplementary Figure S1). Furthermore, there are seven ZnF-A20 motifs in A20/TNFAIP3 and only the fourth is responsible for E3 activity, suggesting that the ZnF-A20 motif is not inherently active enzymatically (Wertz *et al*, 2004). However, we cannot exclude the possibility that ZNF216 may possess DUB or E3 activity highly specific to an unknown substrate without nonspecific or self-ubiquitinylating activity.

ZNF216 likely acts as a bridging or a shuttle factor of ubiquitinylated proteins targeted to the proteasome. Shuttle proteins, such as Rad23p and Dsk2p, share interfaces for ubiquitinylated proteins and the proteasome (Hartmann-Petersen and Gordon, 2004; Elsasser and Finley, 2005).

Although shuttle proteins are required for efficient protein degradation, ectopic expression of hHR23 or hPLIC, the human homologues of Rad23p or Dsk2p, respectively, lead to stabilization of p53 protein (Kleijnen *et al*, 2000; Glockzin *et al*, 2003). These outcomes may be caused by titration effects due to overexpression and are commonly observed following misexpression of shuttle proteins in yeast and mammals (Hartmann-Petersen and Gordon, 2004; Verma *et al*, 2004). Here, we show that ZNF216 has a ubiquitin binding domain and can associate with the 26S proteasome even in the absence of ubiquitin binding, and that overexpression of the zinc-finger protein attenuates protein degradation rate. There is no structural counterpart of ZNF216 in the yeast genome. We asked whether ZNF216 could rescue the bridging function of RAD23 or DSK2 mutants by introducing ZNF216 into Δ*rad23*Δ*dsk2* yeast cells, but the phenotype could not be rescued (data not shown). This suggests that ZNF216 is not the functional orthologue of these proteins. Recently, the presence of an alternative pathway of Rad23p/Dsk2p in protein targeting to the proteasome has been suggested (Bazirgan and Hampton, 2005; Richly *et al*, 2005). It has been reported that tetra-ubiquitin constitutes the minimum proteasomal targeting signal and that the length of polyubiquitin chain may determine the targeting route (Thrower *et al*, 2000; Bazirgan and Hampton, 2005; Richly *et al*, 2005). Notably, ZNF216 preferentially binds polyubiquitin chains longer than di- or tri-ubiquitin (Figure 1D). Therefore, these data suggest that ZNF216 is a novel ubiquitin recognition factor, required for efficient protein degradation via a pathway different from the canonical Rad23p/Dsk2p pathway. Although it is now under investigation, the characterization of ZnF-AN1, an AN1-type zinc-finger domain located at the C-terminus of ZNF216, may reveal the precise molecular function of ZNF216.

Materials and methods

Antibodies

An anti-ZNF216 antibody was raised by immunizing rabbits against synthesized peptide corresponding to the C-terminal sequence of mouse ZNF216. Mouse monoclonal antibodies for FLAG (Sigma, St Louis, MO) and ubiquitin (Santa Cruz Biotechnology, CA), rabbit polyclonal antibodies for ubiquitin (Affiniti Research Products) and actin (Neo Markers, CA), a rat monoclonal antibody for HA (Roche Diagnostics, Mannheim, Germany), and a rabbit polyclonal antibody against S10a/Rpn7p (Affiniti Research Products) were purchased from the indicated manufacturers. For indirect immunofluorescence staining, AlexaFluor 488 goat anti-mouse IgG or AlexaFluor 546 goat anti-rat IgG antibody was obtained from Molecular Probes, OR.

Identification of interacting proteins

RNA was purified from RAW264.7 cells stimulated by RANKL, and used to construct the yeast library (MatchMaker Library Construction & Screening Kit, Clontech). Yeast two-hybrid screening with pGBKT7-ZNF216 was performed as described previously (Masuda *et al*, 2001). Identification of the co-immunoprecipitated proteins with N- or C-terminally FLAG-tagged ZNF216 (ZA20D2) or AWP1 (ZA20D3) was essentially done by a nano-LC/MS/MS system as previously described (Natsume *et al*, 2002; Komatsu *et al*, 2004).

Experimental models of muscle atrophy

For fasting-induced muscle atrophy, 8-week-old C57BL6 male mice were deprived of food but given free access to water. After 2 days, gastrocnemius muscles were harvested for each experiment. Denervation-induced muscle atrophy was performed by dissecting the sciatic nerve of one hindlimb, and the other hindlimb was sham operated as the control. After 7 days, the contralateral normal and denervated gastrocnemius muscles were harvested for each experiment. All animal experiments were approved in advance by the Ethics Review Committee for Animal Experimentation of the National Institute for Longevity Sciences and the National Center for Geriatrics and Gerontology. Student's *t*-tests were used to evaluate statistical differences between the two groups.

Znf216-deficient mice

Generation of heterozygous *Znf216*$^{+/lex}$ mice was essentially done by the gene trap method at Lexicon Genetics (Zambrowicz *et al*, 1998). Briefly, ES cells heterozygous for the trapped *Znf216* gene were microinjected into eight-cell-stage ICR mouse embryos and transplanted into uteri. Chimeric mice were crossed to C57BL/6J mice. Northern and immunoblot analyses confirmed disruption of the gene (see text). For genotyping, primers were as follows: KO-A, ACCGACAGGATAGACAATGGCAGAG; KO-B, CGATTTTAAGAAAG GAGGCTCTGACC; LTR2, AAATGGCGTTACTTAAGCTAGCTTGC. The wild-type and inserted alleles were detected by PCR using KO-A and KO-B (0.5 kb), and LTR2 and KO-B (0.3 kb), respectively.

EGFP-CL1 degradation assay

The nucleotide sequence encoding the CL1 peptide (ACKNWFSSLSHFVIHL) (Gilon *et al*, 1998) was inserted into the *Xho*I/*Eco*RI site of pEGFP-C3, and the resulting plasmid was designated pEGFP-CL1. A cell line stably expressing EGFP-CL1 (293EGFP-CL1) was generated by transfection of pEGFP-CL1 into 293 cells. For the degradation assay, ZNF216 expression vectors were transfected into 293EGFP-CL1 cells and cells were harvested 48 h after transfection. MG132 (final 10 μM) or cycloheximide (final 100 μg/ml) was added to the culture at 12 or 1 h before harvest, respectively. Protein extraction was as described above.

For more details on supplementary Materials and methods, see Supplementary data

Supplementary data

Supplementary data are available at *The EMBO Journal* Online.

Acknowledgements

We are grateful to Drs Kazuhiro Iwai (Osaka City University) and Noboru Motoyama (NCGG) for reagents, helpful comments and suggestions throughout this study. We also thank Drs Akio Matsuda and Tatsuo Furuyama for experimental instruction and advice; Dr Aya Sasaki for pathological determinations; Ms Miho Kamiya and Ms Kumi Tsutsumi for technical assistance; and Dr Elise Lamar for proofreading the manuscript. This study is supported in part by the Program for Promotion of Fundamental Studies in Health Sciences of the Organization for Pharmaceutical Safety and Research of Japan, and by a Research Grant for Longevity Sciences from the Ministry of Health, Labor and Welfare.

References

Anderson DM, Maraskovsky E, Billingsley WL, Dougall WC, Tometsko ME, Roux ER, Teepe MC, DuBose RF, Cosman D, Galibert L (1997) A homologue of the TNF receptor and its ligand enhance T-cell growth and dendritic-cell function. *Nature* **390:** 175–179

Bailey JL, Wang X, England BK, Price SR, Ding X, Mitch WE (1996) The acidosis of chronic renal failure activates muscle proteolysis in rats by augmenting transcription of genes encoding proteins of the ATP-dependent ubiquitin-proteasome pathway. *J Clin Invest* **97:** 1447–1453

Bazirgan OA, Hampton RY (2005) Cdc48-Ufd2-Rad23: the road less ubiquitinated? *Nat Cell Biol* **7:** 207–209

Bence NF, Sampat RM, Kopito RR (2001) Impairment of the ubiquitin-proteasome system by protein aggregation. *Science* **292:** 1552–1555

Bodine SC, Latres E, Baumhueter S, Lai VK, Nunez L, Clarke BA, Poueymirou WT, Panaro FJ, Na E, Dharmarajan K, Pan ZQ, Valenzuela DM, DeChiara TM, Stitt TN, Yancopoulos GD, Glass DJ (2001) Identification of ubiquitin ligases required for skeletal muscle atrophy. *Science* **294:** 1704–1708

Brunet A, Bonni A, Zigmond MJ, Lin MZ, Juo P, Hu LS, Anderson MJ, Arden KC, Blenis J, Greenberg ME (1999) Akt promotes cell survival by phosphorylating and inhibiting a Forkhead transcription factor. *Cell* **96:** 857–868

Cai D, Frantz JD, Tawa Jr NE, Melendez PA, Oh BC, Lidov HG, Hasselgren PO, Frontera WR, Lee J, Glass DJ, Shoelson SE (2004) IKKbeta/NF-kappaB activation causes severe muscle wasting in mice. *Cell* **119:** 285–298

Chen L, Shinde U, Ortolan TG, Madura K (2001) Ubiquitin-associated (UBA) domains in Rad23 bind ubiquitin and promote inhibition of multi-ubiquitin chain assembly. *EMBO Rep* **2:** 933–938

Ciechanover A, Brundin P (2003) The ubiquitin proteasome system in neurodegenerative diseases: sometimes the chicken, sometimes the egg. *Neuron* **40:** 427–446

Elsasser S, Finley D (2005) Delivery of ubiquitinated substrates to protein-unfolding machines. *Nat Cell Biol* **7:** 742–749

Funakoshi M, Sasaki T, Nishimoto T, Kobayashi H (2002) Budding yeast Dsk2p is a polyubiquitin-binding protein that can interact with the proteasome. *Proc Natl Acad Sci USA* **99:** 745–750

Furukawa-Hibi Y, Yoshida-Araki K, Ohta T, Ikeda K, Motoyama N (2002) FOXO forkhead transcription factors induce G(2)-M checkpoint in response to oxidative stress. *J Biol Chem* **277:** 26729–26732

Gilon T, Chomsky O, Kulka RG (1998) Degradation signals for ubiquitin system proteolysis in Saccharomyces cerevisiae. *EMBO J* **17:** 2759–2766

Glickman MH, Ciechanover A (2002) The ubiquitin-proteasome proteolytic pathway: destruction for the sake of construction. *Physiol Rev* **82:** 373–428

Glockzin S, Ogi FX, Hengstermann A, Scheffner M, Blattner C (2003) Involvement of the DNA repair protein hHR23 in p53 degradation. *Mol Cell Biol* **23:** 8960–8969

Gomes MD, Lecker SH, Jagoe RT, Navon A, Goldberg AL (2001) Atrogin-1, a muscle-specific F-box protein highly expressed during muscle atrophy. *Proc Natl Acad Sci USA* **98:** 14440–14445

Hartmann-Petersen R, Gordon C (2004) Protein degradation: recognition of ubiquitinylated substrates. *Curr Biol* **14:** R754–R756

Hershko A, Ciechanover A (1998) The ubiquitin system. *Annu Rev Biochem* **67:** 425–479

Hishiya A, Ikeda K, Watanabe K (2005) A RANKL-inducible gene Znf216 in osteoclast differentiation. *J. Receptor Signal Transduct* **25:** 199–216

Horiuchi H, Lippe R, McBride HM, Rubino M, Woodman P, Stenmark H, Rybin V, Wilm M, Ashman K, Mann M, Zerial M (1997) A novel Rab5 GDP/GTP exchange factor complexed to Rabaptin-5 links nucleotide exchange to effector recruitment and function. *Cell* **90:** 1149–1159

Huang J, Teng L, Li L, Liu T, Li L, Chen D, Xu LG, Zhai Z, Shu HB (2004) ZNF216 is an A20-like and IkappaB kinase gamma-interacting inhibitor of NFkappaB activation. *J Biol Chem* **279:** 16847–16853

Hunter RB, Kandarian SC (2004) Disruption of either the Nfkb1 or the Bcl3 gene inhibits skeletal muscle atrophy. *J Clin Invest* **114:** 1504–1511

Jagoe RT, Lecker SH, Gomes M, Goldberg AL (2002) Patterns of gene expression in atrophying skeletal muscles: response to food deprivation. *FASEB J* **16:** 1697–1712

Johnston JA, Ward CL, Kopito RR (1998) Aggresomes: a cellular response to misfolded proteins. *J Cell Biol* **143:** 1883–1898

Kawaguchi Y, Kovacs JJ, McLaurin A, Vance JM, Ito A, Yao TP (2003) The deacetylase HDAC6 regulates aggresome formation and cell viability in response to misfolded protein stress. *Cell* **115:** 727–738

Kleijnen MF, Shih AH, Zhou P, Kumar S, Soccio RE, Kedersha NL, Gill G, Howley PM (2000) The hPLIC proteins may provide a link between the ubiquitination machinery and the proteasome. *Mol Cell* **6:** 409–419

Komatsu M, Chiba T, Tatsumi K, Iemura S, Tanida I, Okazaki N, Ueno T, Kominami E, Natsume T, Tanaka K (2004) A novel protein-conjugating system for Ufm1, a ubiquitin-fold modifier. *EMBO J* **23:** 1977–1986

Kopito RR (2000) Aggresomes, inclusion bodies and protein aggregation. *Trends Cell Biol* **10:** 524–530

Korhonen L, Lindholm D (2004) The ubiquitin proteasome system in synaptic and axonal degeneration: a new twist to an old cycle. *J Cell Biol* **165:** 27–30

Lacey DL, Timms E, Tan HL, Kelley MJ, Dunstan CR, Burgess T, Elliott R, Colombero A, Elliott G, Scully S, Hsu H, Sullivan J, Hawkins N, Davy E, Capparelli C, Eli A, Qian YX, Kaufman S, Sarosi I, Shalhoub V, Senaldi G, Guo J, Delaney J, Boyle WJ (1998) Osteoprotegerin ligand is a cytokine that regulates osteoclast differentiation and activation. *Cell* **93:** 165–176

Lambertson D, Chen L, Madura K (1999) Pleiotropic defects caused by loss of the proteasome-interacting factors Rad23 and Rpn10 of *Saccharomyces cerevisiae*. *Genetics* **153:** 69–79

Lecker SH, Jagoe RT, Gilbert A, Gomes M, Baracos V, Bailey J, Price SR, Mitch WE, Goldberg AL (2004) Multiple types of skeletal muscle atrophy involve a common program of changes in gene expression. *FASEB J* **18:** 39–51

Lecker SH, Solomon V, Mitch WE, Goldberg AL (1999) Muscle protein breakdown and the critical role of the ubiquitin–proteasome pathway in normal and disease states. *J Nutr* **129:** 227S–237S

Lelouard H, Gatti E, Cappello F, Gresser O, Camosseto V, Pierre P (2002) Transient aggregation of ubiquitinated proteins during dendritic cell maturation. *Nature* **417:** 177–182

Masuda Y, Sasaki A, Shibuya H, Ueno N, Ikeda K, Watanabe K (2001) Dlxin-1, a novel protein that binds Dlx5 and regulates its transcriptional function. *J Biol Chem* **276:** 5331–5338

McKinnell IW, Rudnicki MA (2004) Molecular mechanisms of muscle atrophy. *Cell* **119:** 907–910

Medina R, Wing SS, Haas A, Goldberg AL (1991) Activation of the ubiquitin-ATP-dependent proteolytic system in skeletal muscle during fasting and denervation atrophy. *Biomed Biochim Acta* **50:** 347–356

Mitch WE, Goldberg AL (1996) Mechanisms of muscle wasting. The role of the ubiquitin-proteasome pathway. *N Engl J Med* **335:** 1897–1905

Mitch WE, Price SR (2001) Transcription factors and muscle cachexia: is there a therapeutic target? *Lancet* **357:** 734–735

Natsume T, Yamauchi Y, Nakayama H, Shinkawa T, Yanagida M, Takahashi N, Isobe T (2002) A direct nanoflow liquid chromatography-tandem mass spectrometry system for interaction proteomics. *Anal Chem* **74:** 4725–4733

Opipari Jr AW, Boguski MS, Dixit VM (1990) The A20 cDNA induced by tumor necrosis factor alpha encodes a novel type of zinc finger protein. *J Biol Chem* **265:** 14705–14708

Pickart CM, Cohen RE (2004) Proteasomes and their kin: proteases in the machine age. *Nat Rev Mol Cell Biol* **5:** 177–187

Price SR, Bailey JL, Wang X, Jurkovitz C, England BK, Ding X, Phillips LS, Mitch WE (1996) Muscle wasting in insulinopenic rats results from activation of the ATP-dependent, ubiquitin-proteasome proteolytic pathway by a mechanism including gene transcription. *J Clin Invest* **98:** 1703–1708

Richly H, Rape M, Braun S, Rumpf S, Hoege C, Jentsch S (2005) A series of ubiquitin binding factors connects CDC48/p97 to substrate multiubiquitylation and proteasomal targeting. *Cell* **120:** 73–84

Ross CA, Poirier MA (2004) Protein aggregation and neurodegenerative disease. *Nat Med* **10** (Suppl): S10–S17

Sacheck JM, Ohtsuka A, McLary SC, Goldberg AL (2004) IGF-I stimulates muscle growth by suppressing protein breakdown and expression of atrophy-related ubiquitin ligases, atrogin-1 and MuRF1. *Am J Physiol Endocrinol Metab* **287:** E591–E601

Saeki Y, Saitoh A, Toh-e A, Yokosawa H (2002) Ubiquitin-like proteins and Rpn10 play cooperative roles in ubiquitin-dependent proteolysis. *Biochem Biophys Res Commun* **293:** 986–992

Sandri M, Sandri C, Gilbert A, Skurk C, Calabria E, Picard A, Walsh K, Schiaffino S, Lecker SH, Goldberg AL (2004) Foxo transcription factors induce the atrophy-related ubiquitin ligase atrogin-1 and cause skeletal muscle atrophy. *Cell* **117:** 399–412

Scott DA, Greinwald Jr JH, Marietta JR, Drury S, Swiderski RE, Vinas A, DeAngelis MM, Carmi R, Ramesh A, Kraft ML, Elbedour K, Skworak AB, Friedman RA, Srikumari Srisailapathy CR, Verhoeven K, Van Gamp G, Lovett M, Deininger PL, Batzer MA, Morton CC, Keats BJ, Smith RJ, Sheffield VC (1998) Identification and mutation analysis of a cochlear-expressed, zinc finger

protein gene at the DFNB7/11 and dn hearing-loss loci on human chromosome 9q and mouse chromosome 19. *Gene* **215:** 461–469

Seigneurin-Berny D, Verdel A, Curtet S, Lemercier C, Garin J, Rousseaux S, Khochbin S (2001) Identification of components of the murine histone deacetylase 6 complex: link between acetylation and ubiquitination signaling pathways. *Mol Cell Biol* **21:** 8035–8044

Stitt TN, Drujan D, Clarke BA, Panaro F, Timofeyva Y, Kline WO, Gonzalez M, Yancopoulos GD, Glass DJ (2004) The IGF-1/PI3K/Akt pathway prevents expression of muscle atrophy-induced ubiquitin ligases by inhibiting FOXO transcription factors. *Mol Cell* **14:** 395–403

Tawa Jr NE, Odessey R, Goldberg AL (1997) Inhibitors of the proteasome reduce the accelerated proteolysis in atrophying rat skeletal muscles. *J Clin Invest* **100:** 197–203

Thrower JS, Hoffman L, Rechsteiner M, Pickart CM (2000) Recognition of the polyubiquitin proteolytic signal. *EMBO J* **19:** 94–102

Verma R, Oania R, Graumann J, Deshaies RJ (2004) Multiubiquitin chain receptors define a layer of substrate selectivity in the ubiquitin-proteasome system. *Cell* **118:** 99–110

Wertz IE, O'Rourke KM, Zhou H, Eby M, Aravind L, Seshagiri S, Wu P, Wiesmann C, Baker R, Boone DL, Ma A, Koonin EV, Dixit VM (2004) De-ubiquitination and ubiquitin ligase domains of A20 downregulate NF-kappaB signalling. *Nature* **430:** 694–699

Wilkinson CR, Ferrell K, Penney M, Wallace M, Dubiel W, Gordon C (2000) Analysis of a gene encoding Rpn10 of the fission yeast proteasome reveals that the polyubiquitin-binding site of this subunit is essential when Rpn12/Mts3 activity is compromised. *J Biol Chem* **275:** 15182–15192

Wing SS, Goldberg AL (1993) Glucocorticoids activate the ATP-ubiquitin-dependent proteolytic system in skeletal muscle during fasting. *Am J Physiol* **264:** E668–E676

Wing SS, Haas AL, Goldberg AL (1995) Increase in ubiquitin–protein conjugates concomitant with the increase in proteolysis in rat skeletal muscle during starvation and atrophy denervation. *Biochem J* **307** (Part 3)**:** 639–645

Young P, Deveraux Q, Beal RE, Pickart CM, Rechsteiner M (1998) Characterization of two polyubiquitin binding sites in the 26 S protease subunit 5a. *J Biol Chem* **273:** 5461–5467

Zambrowicz BP, Friedrich GA, Buxton EC, Lilleberg SL, Person C, Sands AT (1998) Disruption and sequence identification of 2000 genes in mouse embryonic stem cells. *Nature* **392:** 608–611

JOURNAL OF BONE AND MINERAL RESEARCH
Volume 20, Number 10, 2005
Published online on June 20, 2005; doi: 10.1359/JBMR.050610

Multi-Detector Row CT Imaging of Vertebral Microstructure for Evaluation of Fracture Risk

Masako Ito,[1] Kyoji Ikeda,[2] Masahiko Nishiguchi,[3] Hiroyuki Shindo,[4] Masataka Uetani,[1] Takayuki Hosoi,[5] and Hajime Orimo[6]

ABSTRACT: We applied MDCT for in vivo evaluation of the microarchitecture of human vertebrae. Microstructure parameters, such as structure model index, Euler's number, and bone volume fraction, revealed higher relative risk for prevalent vertebral fracture than did BMD obtained by DXA. Thus, microstructure analysis by MDCT, together with simultaneously obtained volumetric BMD values, is useful for clinical assessment of fracture risk.

Introduction: BMD measurement by DXA alone has limitations in predicting fracture, and methods for clinical assessment of bone quality, such as microstructure, are awaited. This study was undertaken to examine the applicability of multidetector row CT (MDCT) for in vivo evaluation of trabecular microstructure.
Materials and Methods: Optimal conditions for MDCT scanning were determined at a spatial resolution of 250 × 250 × 500 μm, using μCT data of excised human vertebra specimens as a reference. We analyzed the trabecular microstructure of the vertebrae of 82 postmenopausal women (55–76 years old), including 39 women with and 43 without a recent vertebral fracture.
Results: Microstructure indices obtained by MDCT scanning revealed higher relative risk for prevalent vertebral fracture (OR: 16.0 for structure model index, 13.6 for bone volume fraction, and 13.1 for Euler's number) than did spinal BMD obtained by DXA (OR: 4.8). MDCT could also provide volumetric BMD data, which had higher diagnostic value (OR: 12.7) than did DXA.
Conclusion: Vertebral microarchitecture can be visualized by MDCT, and microstructure parameters obtained by MDCT, together with volumetric BMD, provided better diagnostic performance for assessing fracture risk than DXA measurement.
J Bone Miner Res 2005;20:1828–1836. Published online on June 20, 2005; doi: 10.1359/JBMR.050610

Key words: osteoporosis, fracture, CT, microstructure

INTRODUCTION

BMD MEASUREMENTS ARE widely used for the diagnosis of osteoporosis and for the evaluation of the efficacy of treatment for this disease. However, BMD measurements alone have limitations in predicting fracture. In fact, a recent study indicates that 82% of postmenopausal women with fracture had BMD measurements in the osteopenic, not osteoporotic, range.[1] In addition, there is accumulating evidence that only a small fraction of the reduction in fracture with therapy can be accounted for by the increase in BMD.[2] These results suggest that factors other than BMD, such as bone structure and turnover rate of bone remodeling, contribute to bone fragility.[3]

μCT enables us to evaluate, at an ultra-high resolution, the microstructure of bone samples without destroying them, but it cannot be used in vivo. Studies by high-resolution CT, using different texture analysis methods as well as thresholding techniques, have reported results on its use.[4–6] However, the in-plane spatial resolution of conventional high-resolution CT is only 400 × 400 μm, and this conventional CT only gives information on the characteristic texture of a structure, such as rough versus smooth, homogeneous versus heterogeneous, or high versus low orientation of trabecular distribution. The reason for this is that the trabecular structure is subjected to partial-volume effects. Spiral CT has a higher resolution than conventional CT; however, it is subjected to scan-axis partial volume effects. Multidetector row CT (MDCT) is a new technique that has a substantially higher spatial resolution than standard spiral CT (i.e., it provides an in-plane spatial resolution of 250 μm and a minimum slice thickness of 500 μm) and thus promises to improve the assessment of trabecular bone structure.

The authors have no conflict of interest.

[1]Department of Radiology, Nagasaki University School of Medicine, Nagasaki, Japan; [2]Department of Bone and Joint Disease, The Research Institute, National Center for Geriatrics and Gerontology, Obu, Aichi, Japan; [3]Department of Orthopedic Surgery, Japan Ekisai-kai Nagasaki Hospital, Nagasaki, Japan; [4]Department of Orthopedic Surgery, Nagasaki University School of Medicine, Nagasaki, Japan; [5]Department of Internal Medicine, Tokyo Metropolitan Institute of Gerontology and Geriatric Hospital, Tokyo, Japan; [6]Health Science University, Tokyo, Japan.

This study was undertaken to apply MDCT for 3D imaging of the trabecular microarchitecture of human vertebrae and to evaluate the use of the microstructure parameters obtained by MDCT for the assessment of fracture risk in postmenopausal women.

MATERIALS AND METHODS

Specimen study

Specimens: Five formalin-fixed specimens of vertebrae of female cadavers (62–83 years of age at the time of death) were obtained from Tokyo Metropolitan Institute of Gerontology and Geriatrics Hospital. These vertebrae were used to define the appropriate scanning milli-ampere second value within clinically available values that revealed trabecular microstructure with a low signal-to-noise ratio. To compare the MDCT images with those obtained by μCT, we mounted the excised vertebral specimens on a sample holder of 40 mm diameter filled with an 8% gelatinous solution containing 88% protein, 1% mineral, and 11% water to keep the specimens steady. Specimens that contained air on CT images were excluded. The study protocol was approved by the ethical committee of Tokyo Metropolitan Institute of Gerontology and Geriatrics.

Imaging by μCT: μCT scanning was performed ex vivo on excised human vertebrae to validate MDCT images and data. A μCT apparatus (μCT40) and its analysis software were purchased from SCANCO Medical (Basserdorf, Switzerland).[7] Details of an earlier model (μCT20) were described previously.[8] The process was piloted by an Alpha DS10 workstation (Compaq Computer Corp.), and an open VMS system in a cluster configuration was used to perform 3D analysis. Each specimen was positioned as so to permit scanning of 600 slices with 40-μm increments with a spatial resolution of ~40 μm.

Imaging by MDCT: After μCT scanning, bone specimens in the holder were placed in a 20-cm thickness water-equivalent solid phantom (Standard Grade Solid Water Gammex 457; GAMMEX RMI) and scanned by MDCT. Axial CT images with a collimation of 0.5 mm, a table feed of 2 mm, and a reconstruction index of 0.3 mm were obtained with a MDCT system having four detectors (SOMATOM plus 4 Volume Zoom; Siemens, Erlangen, Germany). An ultra-high spatial resolution kernel was applied (head, filter H 70 very sharp). CT scanning of excised vertebra was performed with the following scanning conditions: field of view (FOV) of 100 mm and pixel matrix of 512 × 512, leading to a maximal spatial resolution of ~250 × 250 × 500 μm^3.

We first determined optimal conditions for MDCT scanning by using excised human vertebrae and compared the MDCT data with those obtained by μCT as a reference. Figure 1 shows images of an excised human vertebra obtained by μCT (Fig. 1A, with the volume of interest shown by a square), high-resolution CT images obtained by MDCT at 200, 250, and 300 mAs (Fig. 1B), their binarized images (Fig. 1C), and reconstructed 3D images (Fig. 1D). Scanning at 350 mAs was not performed because of overload of X-ray tube use for clinical cases. Measurements were repeated at the same position five times, and precision of repeated measurements was 2.35 ± 0.56% for bone volume/total volume (BV/TV), 2.21 ± 2.91% for trabecular number (Tb.N), 3,17 ± 3.28% for trabecular thickness (Tb.Th), 3.62 ± 1.29% for trabecular separation (Tb.Sp), 7.45 ± 1.26% for Euler's number, 4,08 ± 1.48% for structural model index (SMI), and 4.21 ± 1.42% for fractal dimension (n = 3 each).

Structure analysis: Both MDCT image data and μCT data were transferred to a workstation (Precision 360; Dell), and structural indices were calculated using a 3D image analysis system (TRI/3D-BON; RATOC System Engineering Co., Tokyo, Japan). To compare the parameters between μCT images and MDCT images, we defined the volume of interest (VOI) in μCT images first, and then adjusted it for MDCT images with reference to the VOI in μCT images. Grayscale images were segmented by using a median filter to remove noise with a fixed threshold to extract mineralized bone components. We used a standardized method of image thresholding based on the density histogram of a selected region of interest (ROI) to ensure consistency in the image thresholding across all subjects studied. Isolated small particles in the marrow space and isolated small holes in bone were removed by using a cluster-labeling algorithm.

Trabecular microstructure parameters were calculated in 3D as follows: bone volume (BV) was calculated using tetrahedrons corresponding to the enclosed volume of the triangulated surface. Total tissue volume (TV) was the entire volume of analysis, and apparent trabecular bone volume fraction (app BV/TV) was calculated from these values. Apparent trabecular thickness (app Tb.Th) was determined according to the method described by Hildebrand and Ruggsegger.[9] Apparent trabecular number (app Tb.N) and apparent trabecular separation (app Tb.Sp) were estimated based on the plate model.[10]

In addition to the computation of metric parameters, nonmetric parameters were calculated to obtain the 3D nature of the trabecular bone samples. Fractal dimensions of trabecular bone were measured as a representative of complexity using the box-counting method[11] that was developed in 3D. Connectivity was calculated by using the Euler method of Odgaard and Gundersen (Euler's number).[12] Degree of anisotropy (DA) was determined from the ratio between the maximal and minimal radii of the mean intercept length (MIL) ellipsoid.[13]

The interactive analysis time, including data examination, ROI definition, and image segmentation, was ~10 minutes for each type of data.

Biomechanical study

Specimens and microstructure analysis: Four femoral head specimens were obtained during surgery for femoral neck fracture at Nagasaki Rosai Hospital (2 men, 70 and 78 years of age; 2 women, 83 and 85 years of age). Surrounding soft tissues were removed, and 10-mm^3 specimens were prepared and stored at –20°C before use. The study protocol was approved by the ethical committee of Nagasaki Rosai Hospital.

These specimens were placed in an acrylic tank containing physiological saline solution and scanned by MDCT. Scanning direction was adjusted to the direction of loading

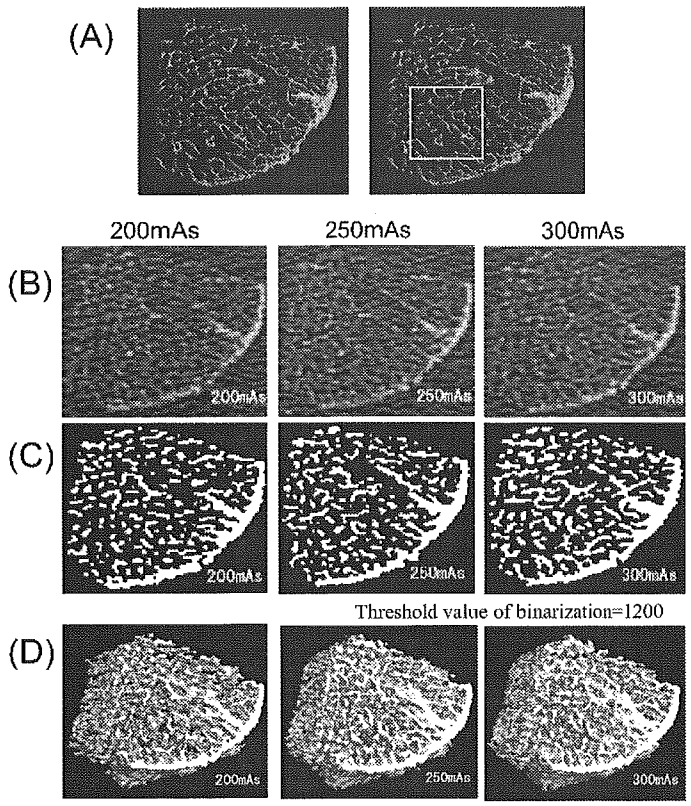

Threshold value	mAs	r	p
1120	200	0.656	ns
	250	0.487	ns
	300	0.959	< 0.01
1200	200	0.665	ns
	250	0.899	< 0.05
	300	0.979	< 0.005
1280	200	0.629	ns
	250	0.886	< 0.05
	300	0.959	< 0.05

FIG. 1. Visualization of spinal microstructure by MDCT scanning. Representative images of excised human vertebrae by (A) μCT image (volume of interest delimited by the square) and (B–D) MDCT images are shown. MDCT images were obtained under different conditions at 200, 250, and 300 mA; each CT image was analyzed at different threshold values (1120, 1200, and 1280). (B) Original 2D MDCT images at 200, 250, and 300 mA. (C) Binarized 2D CT images at 200, 250, and 300 mAs. (D) 3D CT images at 200, 250, and 300 mAs. The binarized and 3D images were prepared by using a threshold value of 1200. The linear correlations (r) and statistical significances (p) between apparent BV/TV measured by μCT and MDCT at 200, 250, and 300 mAs are also shown at the right.

in the biomechanical test. The scanning condition was the same as in the cadaver specimen study described above. Microstructure parameters were obtained for all of the specimens by the same procedure described above.

Determination of bone strength by compression test: Specimens were placed centrally on the compression testing fixture, which is able to hold the specimen stably in the cylinder and load only compressive direction without rotation or bending, and was attached to the materials-testing machine (Instron model 5582). A compression force was applied in a cranio-caudal direction using the fixture at a nominal deformation rate of 0.5 mm/minute and a sampling rate of 20 Hz. Crosshead displacement was recorded as specimen deformation. A load-deformation curve was displayed with a monitoring recorder linked to the tester in each specimen. The ultimate load (kgf) was obtained directly from the load-deformation curve.

Patient study

Patients: Spinal microarchitecture was examined in 82 postmenopausal women (55–76 years old, 65.3 ± 4.8 years) with MDCT scanning. Microstructure parameters were compared between 39 women who experienced their first spinal fracture during the previous 6 months (age: 66.2 ± 3.8 years old) and 43 women without fracture (age: 64.4 ± 5.5 years old) to assess the correlation between these parameters and fracture. Spinal fracture was defined according to the criteria proposed by Genant et al.[14] (i.e., vertebral deformity was considered as a fracture when at least a 20% reduction in anterior, middle, and/or posterior height and a 10% reduction in area were observed). Individuals who had had an osteoporotic fracture 6 months or more before the study were excluded, because bone structure would have been altered by the fracture. None of the postmenopausal women had received drugs affecting bone mass or bone metabolism within 6 months before the study. Nagasaki University ethics committee approved the protocol, and all subjects (i.e., fracture cases and controls) gave their informed consent.

BMD measurements: BMD of the lumbar spine (L_2–L_4) in antero-posterior (AP) projection was determined using DXA, and fractured vertebrae were excluded from the analysis. The obtained values were expressed as units of grams per centimeter squared for the projected area. Expert-EL (Lunar Corp., Madison, WI, USA) was used to measure the BMD of the lumbar spine. The CV (short-term precision) for L_2–L_4 was 1.1%.

To obtain volumetric BMD data by QCT, we scanned the patients simultaneously with MDCT using a bone mineral reference phantom (B-MAS2000; KYOTOKAGAKU Co.,

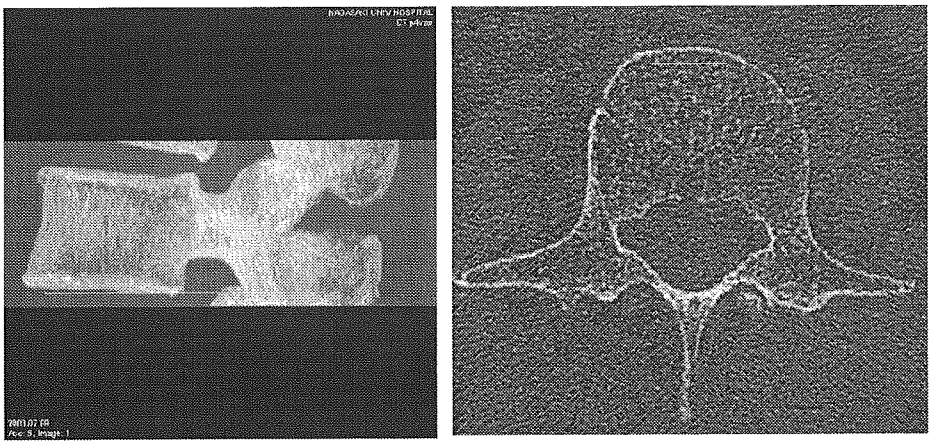

(A) (B)

FIG. 2. ROI for analysis of trabecular microstructure by MDCT. (A) The whole third lumbar spine including both endplates was scanned by MDCT. (B) The volume of interest (VOI) of 65 × 65 pixels in plane was defined in the anterior part of the spongiosa (delimited by the square) to avoid cortex and the basivertebral foramen.

Kyoto, Japan) containing calibration objects with equivalent densities of 0, 50, 100, 150, and 200 mg/cm^3 calcium hydroxyapatite. Reconstructed stacked 3D volume data of the vertebral body with reference phantom were used for the determination of volumetric BMD. VOI was defined in the same region for microstructure measurement of the reconstructed vertebral CT image.

Imaging by MDCT and structure analysis: The whole third lumbar spine including both endplates was scanned by MDCT, as shown in Fig. 2A. Patients were in the supine position for horizontal scanning of the vertebral body. The vertebral body was scanned under the appropriate X-ray condition, which was determined in the ex vivo cadaver study as described above. For the analysis of microstructure, the size of the VOI of 65 × 65 pixels in plane was defined (Fig. 2B); the total number of slices varied according to the size of the vertebral body. The VOI was defined manually within the internal part of the cancellous bone to avoid the cortex, the basivertebral foramen, and both endplates. The midline of the VOI in the x-axis in the axial image was in the center of the vertebral body, and the frontal edge on both sides of the VOI was just behind the cortex. The average number of slices was 43.8 ± 5.3 (range, 28–52 slices).

The procedure for structure analysis was the same as that for the cadaver specimen study described above. Samples from three patients were scanned five times on different days, using manually defined VOI; the precision was confirmed by the same operator. Precision of measurements of microstructure parameters was 0.67% for fractal dimension, 0.84% for Tb.Th, 1.13% for SMI, 2.04% for DA, 6.57% for Tb.N, 7.13% for BV/TV, 7.36% for Tb.Sp, and 12.30% for Euler's number.

Statistical analysis

Data analysis was performed with the software statistical package for Social Science, SPSS (SPSS, Chicago, IL, USA). Mean and SD of microstructure parameters and BMD were calculated for the postmenopausal women with or without fracture. The significance of differences between the two groups was calculated by ANOVA and posthoc test (Fisher's protected least significant difference [PLSD]), at the 95% significance level. Correlations of microstructure parameters or BMD with age or body weight of the subjects and correlations between microstructure parameters and BMD were assessed using linear regression analysis. Area under the curve (AUC) in receiver operator characteristic (ROC) analysis was generated to determine the diagnostic efficacy for detection of fracture cases. Additionally, the ORs per SD were calculated by logistic regression analysis to provide an estimate for the discriminatory capability of each variable for spinal fracture, as a single parameter or in combination with DXA or QCT value.

RESULTS

Specimen study

Optimal conditions for MDCT scanning: To determine the optimal conditions for MDCT scanning, we obtained vertebral specimens from cadavers and scanned them by both μCT (Fig. 1A) and MDCT (Figs. 1B–1D). Microstructure parameters were calculated at threshold values of 1120, 1200, and 1280 to binarize bone CT images. These values of threshold were numbers on a scale from 0 to 4290 according to linear attenuation, which has no units. As shown in Fig. 1 (right), at all three threshold levels, BV/TV obtained by μCT revealed the highest correlation with app BV/TV by MDCT at 300 mAs (r = 0.979, $p < 0.005$ at a threshold value of 1200).

When scanned at 0.5 mm thickness, 71-mm scan length, 0.8 feed/rotation, and 120 kVp, weighted CT dose indices (CTDIw) were 46.3 mGy for 200 mAs, 59.1 mGy for 250 mAs, and 77.1 mGy for 300 mAs.

Correlation between microstructure parameters and biomechanical properties: To examine whether microstructure parameters correlate with biomechanical properties, another set of four specimens were obtained from the femoral head at surgery and subjected to compression test after scanning by μCT and MDCT. As shown in Fig. 3, microstructure parameters obtained by MDCT revealed a high correlation with ultimate load (kgf); a significant correlation with the ultimate load was obtained for app BV/TV ($p < 0.05$), SMI ($p < 0.05$), and app Th.N ($p < 0.05$).

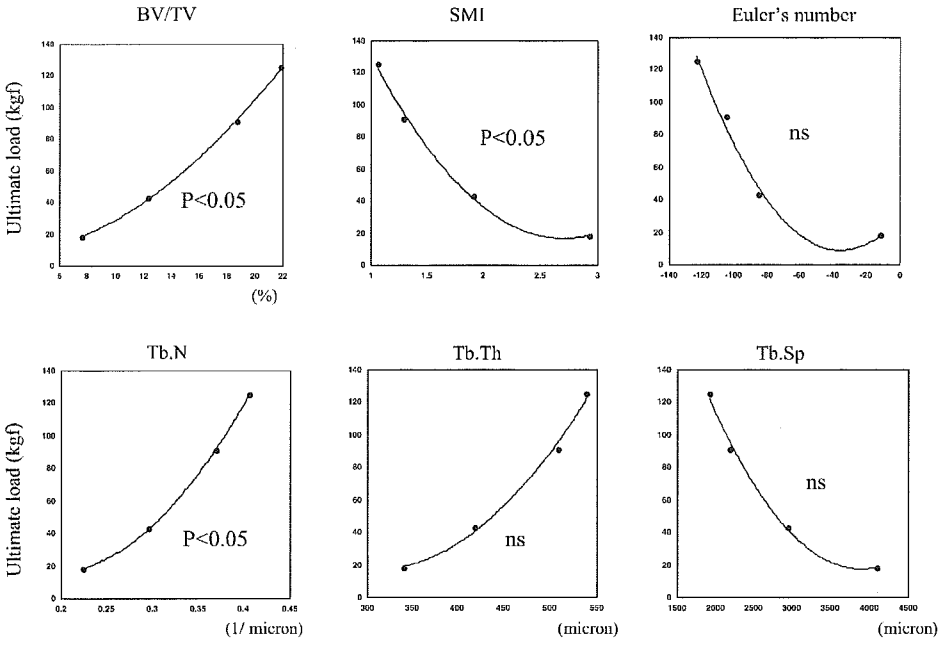

FIG. 3. Correlation between microstructure parameters and bone strength. Ten-millimeter cubic specimens were obtained from the femoral head of four individuals and scanned by μCT and MDCT. Structure analysis was performed as described in the Materials and Methods section. The specimens were subjected to biomechanical test, and the ultimate load was obtained from the load-deformation curve. Shown are significant correlations between microstructure parameters obtained by MDCT and bone strength. p values are shown for each parameter.

Patient study

Association of microstructure parameters with prevalent spinal fracture: To examine the use of trabecular microarchitecture information obtained by MDCT scanning for the assessment of fracture, we compared the microstructure parameters derived from MDCT images between 43 women without fracture (age: 64.4 ± 5.5 years old) and 39 women with a recent spinal fracture (age: 66.2 ± 3.8 years old). As shown in Table 1, there was no significant difference in age, age at menopause, body height (BH), or body weight (BW) between these two groups of women.

Figures 4A–4F show representative 2D (Figs. 4A and 4B), its binarized 2D (Figs. 4C and 4D), and 3D (Figs. 4E and 4F) MDCT images of the third lumbar vertebra of a 62-year-old woman without vertebral fracture (Figs. 4A, 4C, and 4E) and those of a women of the same age with a fracture in the thoracic spine (Figs. 4B, 4D, and 4F).

Table 1 summarizes the results of microstructure parameters, as well as areal (by DXA) and volumetric (by MDCT) BMD values in the two groups of women. Areal BMD by DXA was significantly lower in postmenopausal women with a fracture than in those without one (0.836 ± 0.191 versus 0.925 ± 0.161 g/cm^2, $p < 0.05$). Among the microstructure indices obtained by MDCT, app BV/TV, app Tb.N, app Tb.Th, and fractal dimension were significantly lower; whereas app Tb.Sp, SMI, Euler's number, and DA were significantly higher in women with a fracture than in those without a fracture (Table 1). Volumetric BMD determined by MDCT was also significantly lower in postmenopausal women with a fracture (72.0 ± 18.5 versus 103.9 ± 23.5 mg/cm^3, $p < 0.0001$).

Table 2 shows the correlation of microstructure parameters with BMD values obtained by DXA and QCT. Most microstructure parameters were more highly correlated with volumetric BMD by QCT than with areal BMD by DXA.

ROC analysis was performed to determine the diagnostic value of microstructure parameters with respect to fracture (Table 3). The highest AUC value was obtained for SMI (0.928), which was significantly higher than that for areal BMD by DXA (0.647) or volumetric BMD by MDCT (0.870). AUC values of Euler's number (0.857) and app Tb.Sp (0.818) were similar to that value of volumetric BMD, and significantly exceeded that of areal BMD by DXA. The ORs for the association of SMI (16.0), app BV/TV (13.6), Euler's number (13.1), app Tb.Sp (7.4), fractal dimension (7.4), app Tb.N (6.6), and app Tb.Th (5.5) with fracture were higher than the OR for that of areal BMD by DXA with it (4.8); the ORs for SMI, app BV/TV, and Euler's number exceeded that ratio of volumetric BMD (12.7). Multivariate regression analysis showed significant correlations of SMI (R^2 = 0.329, $p < 0.0001$) and Tb.Th (R^2 = 0.154, $p < 0.005$), as well as volumetric BMD (R^2 = 0.159, $p < 0.005$), with fracture (Table 4). Combining areal or volumetric BMD data with some microstructural parameters further increased R^2 values compared with BMD alone (Table 4).

Table 5 shows the correlations of spinal microarchitecture or BMD with age and BW. Most microstructure parameters and volumetric BMD by MDCT correlated with age, especially SMI, Euler's number, and app BV/TV, whereas areal BMD values by DXA showed a moderate correlation with both age and BW.

DISCUSSION

The purpose of this study was to evaluate the diagnostic value of in vivo analysis of spinal trabecular microstructure, focusing on its association with prevalent spinal fracture. Compared with postmenopausal women without a spinal fracture, those with one had a smaller trabecular bone fraction (app BV/TV: 36.1 versus 26.2) in association with fewer

TABLE 1. COMPARISON OF VERTEBRAL MICROSTRUCTURAL PARAMETERS BETWEEN TWO GROUPS WITHOUT AND WITH FRACTURE

	Without fracture (n = 43)	*With fracture (n = 39)*	*p (by t-test)*
Background data			
Anthropometric data			
Age (years)	64.4 ± 5.5	66.2 ± 3.8	NS
Age at menopause (years)	50.3 ± 2.8	48.9 ± 4.2	NS
Body height (cm)	152.3 ± 4.7	150.1 ± 7.2	NS
Body weight (kg)	52.8 ± 7.3	50.1 ± 7.8	NS
Areal BMD by DXA (g/cm^2)	0.925 ± 0.161	0.836 ± 0.191	0.05
MDCT data			
Microstructure parameters			
App BV/TV (%)	36.1 ± 7.0	26.1 ± 8.5	<0.0001
App Tb.N ($1/mm^3$)	0.97 ± 0.09	0.78 ± 0.20	<0.0001
App Tb.Th (μm)	368.3 ± 46.1	335.8 ± 46.2	0.005
App Tb.Sp (μm)	667 ± 129	1064 ± 439	<0.0001
Structure model index	1.87 ± 0.48	2.70 ± 0.38	<0.0001
Euler's number	−1037 ± 375	−457 ± 404	<0.0001
Fractal dimension	2.52 ± 0.06	2.41 ± 0.18	0.0005
Degree of anisotropy	1.44 ± 0.15	1.58 ± 0.35	0.05
Volumetric BMD (mg/cm^3)	103.9 ± 23.5	72.0 ± 18.5	<0.0001

Data are shown as mean ± SD.

app BV/TV, apparent bone volume fraction; app Tb.N, apparent trabecular number; app Tb.Th, apparent trabecular thickness; app Tb.Sp, apparent trabecular separation; NS, not significant.

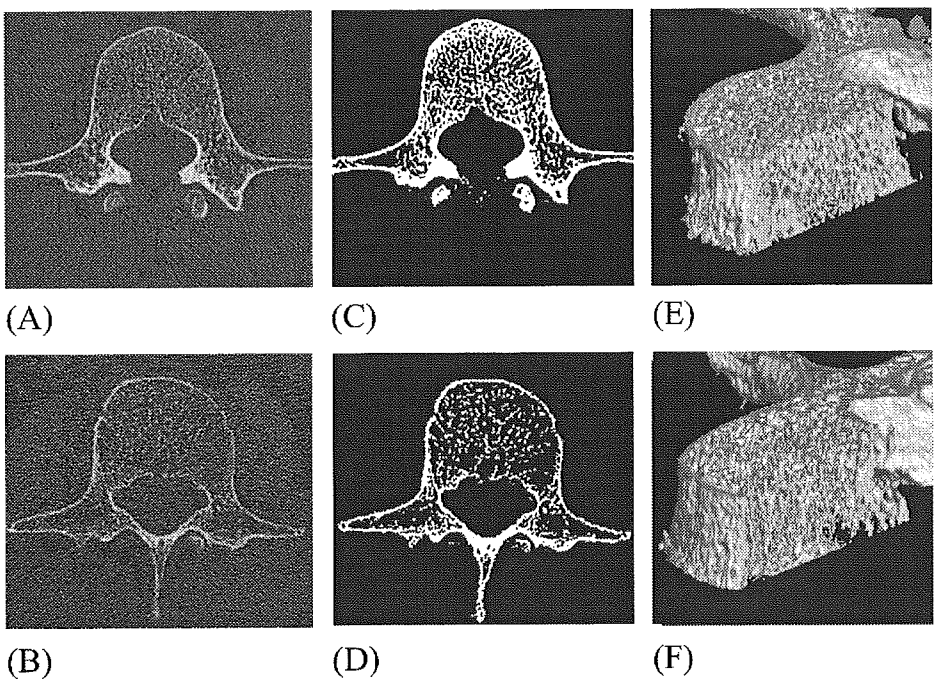

FIG. 4. Representative 2D and 3D MDCT images of the third lumbar spine. (A and B) 2D and (E and F) 3D MDCT images of the third lumbar spine were obtained from (A and E) a 62-year-old woman without vertebral fracture and (B and F) a woman of the same age with a vertebral fracture in her thoracic spine. (C and D) Binarized images are also shown.

trabeculae (app Tb.N: 0.97 versus 0.78), more rodlike structure (SMI: 1.87 versus 2.70), and lower connectivity (Euler's number: −1037 versus −457). The ORs of microstructure parameters, such as SMI, Euler's number, and app BV/TV, for association with prevalent fracture were much higher than that ratio for association of areal BMD by DXA with it. SMI and Euler's number, which represent nonmetric features of trabecular structure, would seem to be more useful than metric parameters such as app Tb.N, app Tb.Th, or app Tb.Sp. It is an advantage of the MDCT scanning system that, in addition to assessing these 3D microstructure parameters, volumetric BMD values can be obtained at the same time by using a reference phantom; these values correlate highly with the presence of fracture.

In vivo analysis of trabecular microstructure has been studied using conventional radiography, high-resolution CT, and high-resolution MRI. Conventional radiography has a spatial resolution of up to 40 μm; however, it delivers projectional images of the trabecular structure. Conventional high-resolution CT with spatial resolution of 400 μm shows only structural texture, because the trabecular structure is subjected to partial-volume effects. With the use of

Journal of Receptors and Signal Transduction, 25:199–216, 2005

ISSN: 1079-9893 print / 1532-4281 online
DOI: 10.1080/10799890500240781

Taylor & Francis
Taylor & Francis Group

A RANKL-Inducible Gene *Znf216* in Osteoclast Differentiation

Akinori Hishiya, Kyoji Ikeda, and Ken Watanabe

Department of Bone and Joint Disease, National Center for Geriatrics and Gerontology (NCGG), Obu, Aichi, Japan

Osteoclasts possess catabolic activity in mineralized tissues and are involved in bone remodeling coordinating with osteoblasts. Although the pathway using receptor and activator of NF-κB (RANK) and its ligand, RANKL, is known to be essential for osteoclast differentiation, their precise mechanisms are not fully understood. Using DNA microarray technology, we searched for genes that were up-regulated after RANKL stimulation in the macrophage cell line, RAW264.7 cells. A gene, *Znf216,* which encodes a zinc-finger protein, was detected among those genes up-regulated after RANKL stimulation. Expression of *Znf216* was also induced by other cytokines such as TNFα and IL-1β. Although ectopic expression of full-length ZNF216 abrogated osteoclast differentiation, its truncated forms accelerated it. No significant inhibitory effect on the NF-κB pathway was observed, however. These results suggest that ZNF216 is a potent inhibitory factor for osteoclast differentiation and that the mechanism is unlikely due to direct attenuation of the NF-κB pathway.

Key Words: RANKL; cDNA microarray; ZNF216

INTRODUCTION

Osteoclasts are multinucleated giant cells derived from the hematopoietic lineage (1). A number of extracellular factors expressed at distinct stages are involved in osteoclast differentiation (2,3). For example, studies in the *op / op* mice, which are severely osteopetorotic due to the absence of osteoclasts, revealed that M-CSF plays a critical role in osteoclast differentiation (4). Proinflammatory cytokines, such as TNFα and IL-1β also accelerate osteoclast differentiation (5,6).

Address correspondence to Ken Watanabe, PhD, Department of Bone and Joint Disease, National Center for Geriatrics and Gerontology (NCGG), 36-3 Gengo, Morioka-cho, Obu, Aichi 474-8522, Japan. Tel: +81-562-46-2311; Fax: +81-562-44-6595; E-mail: kwatanab@nils.go.jp

Among the cytokines, the essential key regulator for osteoclast differentiation is a TNF family cytokine, RANKL (7,8). Mice lacking RANKL or its receptor, RANK, display severe osteopetorosis with a complete absence of osteoclasts, suggesting that the RANKL-RANK pathway is indispensable for osteoclast differentiation (9,10). This pathway promotes not only osteoclast differentiation but also activation (7) and survival (11).

The intracellular signaling events that mediate osteoclast differentiation have been studied by using genetic approaches. Double knockout mice of the p50 and p52 subunits of the transcription factor, NF-κB, display osteopetrosis as seen in RANKL null mice (12). NF-κB functions downstream of the RANKL-RANK pathway and presumably activates genes necessary for osteoclast differentiation. Knockout mice for *fos*, a member of the AP-1 family, also exhibit osteopetorosis (13). c-Fos is thought to be activated by the RANKL-RANK pathway, although the precise mechanism of action remains unknown (14). In addition, src kinase is activated by the RANKL-RANK pathway, and even though src-deficient mice display normal number of osteoclasts, their resorption activity is impaired (15,16). Src is known to be localized to ruffled border membranes, where bone resorption takes place (17). Collectively, these results show that a number of signaling molecules are involved in RANKL-induced osteoclast differentiation and function, although the downstream and the regulatory mechanism have not been fully elucidated.

In the present study, we used cDNA microarray technology to elucidate changes in gene expression during osteoclast differentiation. Among the genes up-regulated, *znf216* is also activated by proinflammatory cytokines, such as TNFα and IL-1β. Furthermore, overexpression of ZNF216 strongly inhibits RANKL-induced osteoclast differentiation. Thus, novel negative regulation may exist for osteoclast differentiation downstream of RANKL stimulation.

MATERIALS AND METHODS

Antibodies and Reagents

Anti-ZNF216 antibody was raised against a synthesized peptide corresponding to the C-terminal sequence of mouse ZNF216 (amino acids 200–213). Mouse monoclonal antibodies for FLAG (M2 and M5) and tubulin (B-5-1-2) were purchased from Sigma (St. Louis, MO, USA). Antibodies against IκBα (C-21), p50 (C-19), p52 (C-5), and p65 (A) were obtained from Santa Cruz Biotechnology (Santa Cruz, CA, USA). RANKL, TNFα, and IL-1β were purchased from R&D Systems (Minneapolis, MN, USA). Lipopolysaccharide (LPS) and TPA (12-*O*-tetradecanoylphorbol-13-acetate) were purchased from Sigma and IFNγ from Genzyme (Cambridge, MA, USA).

Cell Culture Transfection

RAW264.7 mouse monocyte/macrophage cells were maintained in α-modified Eagle's medium (αMEM) containing 10% heat-inactivated fetal bovine serum (FBS) supplemented with penicillin, streptomycin, and L-glutamate. For in vitro osteoclastogenesis, RAW264.7 cells were plated at a density of $1.3 \times 10^4/cm^2$ and incubated overnight. Recombinant mouse RANKL was then added to a final concentration of 10 ng/mL. To detect tartrate-resistant acid phosphatase (TRAP) activity, a hallmark of osteoclasts, cells were fixed with an acetone-citrate-formalin solution (65:27:7) and stained by using a leukocyte acid phosphatase kit (Sigma Diagnostics). For isolation of RNA, RAW264.7 cells were stimulated with TNFα (10 ng/mL), IL-1β (10 ng/mL), LPS (10 μg/mL), TPA (1 mM), or IFNγ (100 U/mL), and harvested at the indicated time points. RANK293 cells, which constitutively express RANK, were kindly provided by Drs. Naoki Sakurai (Tanabe Seiyaku Co., Ltd., Osaka, Japan) and Kunihiro Matsumoto (Nagoya University, Japan) (18). HEK293 and RANK293 cells were cultured at 37°C in Dulbecco's modified Eagle's medium (DMEM) containing 10% heat-inactivated FBS supplemented with penicillin and streptomycin. FuGENE6 (Roche Diagnostics, Mannheim, Germany) was used for transfection. RAW264.7 cells stably expressing full-length or truncated forms of ZNF216 were established by infection using Pantropic Retroviral Expression System (Clontech Laboratories, Palo Alto, CA, USA) and maintained in media containing puromycin.

Isolation of RNA and cDNA Microarray

Total RNA was isolated from RAW264.7 cells at 24, 48, and 72 hr after addition of RANKL. Untreated RAW264.7 cells were used as $t = 0$ hr control. Total RNA was purified by using TRIZOL Reagent (Invitrogen, Carlsbad, CA, USA), according to the manufacturer's instructions. Purification of mRNA was performed by using Micro-Fast Track 2.0 (Invitrogen). Purified mRNA was subsequently used for cDNA microarray analyses (Mouse GEM-I, Incyte Genomics, Palo Alto, CA, USA).

Plasmid Construction

Full-length ZNF216 cDNA was amplified by reverse transcription-coupled PCR (RT-PCR) and subcloned into pBabe-puro retrovirus vector or pEF4 /Myc-HisA (Invitrogen) with a FLAG epitope tag at the N-terminus to generate pF-ZNF216. Zinc finger-deleted mutants, ZNF216ΔN (amino acids 36–213) and ZNF216ΔC (amino acids 1–153), were also generated by PCR and subcloned into the vectors. All cDNAs and constructs amplified by PCR were fully sequenced (ABI PRISM^{TM} 3100 Genetic Analyzer, Applied Biosystems, Foster City, CA, USA).

Northern Blot Analysis

Total RNA was denatured by glyoxal/dimethylsulfoxide and electrophoresed on a 0.9% agarose gel and transferred to a nylon membrane (Amersham Biosciences, Little Chalfont, Buckinghamshire, England). To detect the indicated mRNA, cDNA was labeled with ^{32}P with use of DNA labeling beads (Amersham Biosciences).

Immunoblot Analysis

For chasing IκBα degradation, cells were lyzed in lysis buffer (50 mM Tris-HCl, 150 mM NaCl, 1.0% NP-40, 0.5% sodium deoxycholate, 0.1% SDS, pH7.5). Aliquots of lysates were separated by SDS-PAGE and immunoblotted. Visualization was done by ECL Plus reagents (Amersham Biosciences). For nuclear translocation of NF-κB, cells were lyzed and suspended in hypotonic buffer (50 mM HEPES-KOH, 10 mM KCl, 0.1 mM EDTA, 0.1% NP-40, and protease inhibitor cocktail, pH7.8). Nuclei were pelleted by centrifugation, and the cytosolic fraction was removed. The nuclei were resuspended in extraction buffer (50 mM HEPES-KOH, 420 mM KCl, 0.1 mM EDTA, 5 mM $MgCl_2$, 2% glycerol, and protease inhibitor cocktail, pH7.8), and rotated for 30 min in 4°C. The samples were centrifuged to remove debris. Protein content was measured by using BCA protein assay reagent (PIERCE, Rockford, IL, USA).

Electrophoretic Mobility Shift Assay (EMSA)

EMSA was performed as described by Yousef with minor modification (19). Briefly, RANK293 cells treated with RANKL were washed with ice-cold PBS, and then nuclear extracts were prepared as described above. Ten micrograms of the nuclear extract were incubated with an end-labeled double-stranded oligonucleotide probe containing the sequence 5′-AAA CAG GGG GCT TTC CCT CCT C-3′ derived from the κB3 site of the TNF promoter. The reaction was performed in a total of 20 μL of binding buffer (10 mM HEPES-KOH, 50 mM KCl, 1 mM EDTA, 5 mM $MgCl_2$, 3 μg poly dI-dC, and 10% glycerol, pH7.8) for 30 min at room temperature. Samples were then fractionated in a 4% polyacrylamide gel and visualized by exposing the dried gel to film.

Reporter Gene Assay

HEK293 cells were seeded onto 24-well culture plates and transfected with 10 ng pNF-κB-Luc plasmid (Stratagene, La Jolla, CA, USA), and 5 or 25 ng of ZNF216 full-length or mutant-expressing plasmid. Twenty-four hours after transfection, cells were incubated with low-serum-containing medium (0.5% FBS) for 24 hr, and then TNFα (100 ng/mL) was added. 24 hr after the addition of the cytokine, cells were harvested. For AP-1 reporter gene assays, 100 ng

pAP1-Luc plasmid (Stratagene) was transfected with or without 250 ng ZNF216 full-length-expressing plasmid. AP-1 activation was conducted by using 10 ng pFC-MEKK positive control plasmid (Stratagene). In all transfection experiments, 10 ng Renilla luciferase expression vector, phRG-TK (Promega, Madison, WI, USA), was used as an internal control and for normalization of transfection efficiency. The luciferase activity was measured by using the Dual-Luciferase Reporter Assay System (Promega).

RESULTS

Gene Expression Profile of RANKL-Induced Osteoclast Differentiation

RANKL-treated RAW264.7 cells were efficiently differentiated to osteoclast-like cells (OCLs) within 4 days, as evidenced by multiple nuclei and expression of the osteoclast marker, TRAP (not shown). Isolated RNAs were applied to a cDNA microarray to determine the relative expression levels of about 10,000 mouse genes in response to RANKL stimulation. Analyses revealed that 208 genes were up-regulated, and 515 genes were down-regulated, more than 1.7-fold for at least one time point over a 72-h time-course. A select list of genes differentially expressed are listed in Tables 1 and 2. Genes characteristic for osteoclasts, such as vacuolar ATPases, carbonic anhydrases, and matrix metalloproteinase 9, were up-regulated (Table 1), whereas macrophage-related genes, such as lysozyme and macrophage expressed gene 1, were prominently down-regulated (Table 2). These data collectively suggest that the profiling represents the transition of macrophages into osteoclasts. Among the up-regulated genes, those encoding transcription factors were evident, including c-myc and NFATc1. It was previously reported that c-myc was strongly induced by RANKL and that a dominant negative form of c-myc suppressed osteoclast differentiation (20), suggesting c-myc as a transcription factor involved in the promotion of osteoclastogenesis under the RANKL-RANK pathway. NFATc1 was also shown to be a downstream gene of c-fos, which is known to be activated by RANKL, and osteoclastogenesis of precursor cells of c-Fos$^{-/-}$ mice was rescued by forced expression of the active form of NFATc1 (21).

Another interesting finding was the down-regulation of interferon-induced genes. Takayanagi et al. (22) showed that IFNγ was a potent inhibitor of osteoclastogenesis. Treatment of RAW264.7 cells with IFNγ resulted in rapid degradation of the adaptor protein, TRAF6, via the ubiquitin-proteasome system. The expression of STAT1, which is activated by IFNγ, was also suppressed by RANKL. These results suggest that interferon itself or a pivotal transcription factor for interferon signaling, such as STAT1, is down-regulated during RANKL-induced osteoclastogenesis.

Table 1: Genes up-regulated during RANKL-induced osteoclast differentiation. Fold increase compared to $t = 0$ at the indicated time points is shown.

Gene description	UniGene ID	Fold		
		24 hr	48 hr	72 hr
Bone resorption				
Vocuolar ATPase catalytic subunit A	Mm.29771		1.9	2.4
ATPase-like vacuolar proton channel	Mm.30155	1.7	2.1	2.5
Carbonic anhydrase 1	Mm.3471		1.9	
Carbonic anhydrase 2	Mm.1186	1.5	1.7	2.3
Matrix metalloproteinase 9	Mm.4406		2.0	1.5
Signaling				
TRAF1	Mm.12898		2.5	1.6
TRAF5	Mm.196445		2.0	
skp2	Mm.35584		3.0	1.4
Transcription				
NFATc1	Mm.329560		3.2	1.8
Myc	Mm.2444	3.1	2.1	1.5
Fra2	Mm.24684	3.7	2.7	2.6
forkhead box G1	Mm.4704		3.2	
NF-kB2	Mm.102365	2.3		
Gbx2	Mm.204730		1.9	
Hoxa2	Mm.131		2.6	
Cytokine				
IL-15	Mm.4392		2.0	1.4
PDGF	Mm.2675		2.4	
Small inducible cytokine A9	Mm.2271		2.7	2.1
Other				
Aldose reductase	Mm.451			2.7
Butyrate response factor 1	Mm.18571	1.9	1.7	1.7
DNA polymerase epsilon, subunit 2	Mm.9199		3.0	
GABA-A transporter 2	Mm.22562	1.3	1.7	2.0
H1-0 histone	Mm.24350		2.5	
gly96	Mm.25613		2.2	2.2
slug	Mm.4272		2.7	
ZNF216	Mm.292405		3.0	2.2

Expression of ZNF216 in RANKL-Induced Osteoclast Differentiation

Microarray results also indicated that the gene encoding ZNF216 was potently induced by RANKL. Although *znf216* was first identified as a candidate gene that might be involved in autosomal recessive nonsyndromic hearing loss (ARNSHL), neither disease-causing mutations nor abnormal expression of the gene was found (23). To verify the cDNA microarray results, we carried out Northern blot analysis. The entire coding region of ZNF216 was used as a probe recognizing 2.4-kb and 1.5-kb mRNA species, derived from alternative splicing and polyadenylation. Both species were up-regulated by RANKL as early as 1 hr and peaked 48 hr after addition of the cytokine (Fig. 1A). As shown in Figure 1B, induction of the protein was confirmed by immunoblotting using anti-ZNF216 antibody. An approximately 32-kDa protein was recognized and increased dramatically after RANKL stimulation. Although the expression

Table 2: Genes down-regulated during RANKL-induced osteoclast differentiation. Fold decrease compared to $t = 0$ at the indicated time points is shown.

Gene description	UniGene ID	Fold		
		24 hr	48 hr	72 hr
Macrophage-related				
Lysozyme	Mm.45436		−29.6	−11.4
Macrophage expressed gene 1	Mm.3999	−4.6	−3.3	−3.9
β2 microglobuline	Mm.163		−2.4	−2.7
Fc receptor IgE	Mm.22673		−2.5	−1.8
Fc receptor IgG high affinity I	Mm.150		−3.4	−2.8
Histocompatibility 2 L region	Mm.260691		−1.9	−1.4
Histocompatibility 2 Q region	Mm.34421		2.4	−2.1
Histocompatibility 2 T region	Mm.221296		−2.2	−2.3
Signaling				
Adenylate cyclase 7	Mm.288206	−1.3	−2.0	−1.6
Adenylate cyclase-associated CAP protein	Mm.8687		−3.5	−3.0
Calmodulin 2	Mm.18041		−1.9	−1.5
STAT 1	Mm.8249		−2.2	−2.3
JAK2	Mm.809	−2.2		
Ribosomal protein S6 kinase, polypeptide 4	Mm.20914		−2.1	
MAPK14	Mm.4437		−1.7	−2.2
MAPKKK1	Mm.15918		−2.0	−1.5
AMP-dependent protein kinase	Mm.16766	−1.7	−1.9	−2.1
fyn proto-oncogene	Mm.4848		−1.6	−2.0
Cell cycle and differentiation				
Id2	Mm.34871		−3.8	−2.2
Id3	Mm.110		−2.0	−2.5
cyclin D1	Mm.273049		−1.6	−2.3
cdk2	Mm.118			−2.0
p21	Mm.34446	−1.3	−1.7	−2.5
Matrix protein and secreted-protein related				
ADAM15	Mm.19830		−1.9	−2.0
ADAM17	Mm.355306		−2.2	−1.8
IGF-1	Mm.268521	−3.6	−2.2	
IGF-1 binding protein 4	Mm.233799		−2.2	−2.3
Osteopontin	Mm.288474	−2.6	−4.0	−1.6
Interferon induced gene				
Interferon activated gene 203	Mm.261270	−2.2	−2.1	−2.0
Interferon activated gene 204	Mm.212870		−2.5	
Interferon dependent positive acting transcriptio factor 3	Mm.2032		−1.8	−2.0
Interferon γ inducible protein	Mm.24769		−2.0	−1.5
Interferon regulatory factor 5	Mm.6479		−2.0	−2.0
Interferon regulatory factor 7	Mm.3233		−3.8	−3.0
Interferon induced protein with tetratricopeptide repeat 3	Mm.271850		−1.5	−2.4
2′-5′ oligoadenylate synthetase 1A	Mm.14301	−1.5	−3.6	−1.4
Lysosomal protein				
Cathepsin D	Mm.231395		−3.0	−2.3
Cathepsin L	Mm.930	−1.5	−4.8	−5.9
Cathepsin S	Mm.3619	−2.4	−2.6	−2.1
Lysosomal membrane glycoprotein 2	Mm.486		−2.4	−1.7
Other				
Annexin A2	Mm.238343		−1.6	−2.1
Caspase 1	Mm.1051	−1.7	−1.5	−2.6
Coronin	Mm.27317	−1.7	−2.4	−2.1
Amyloid beta precursor protein	Mm.277585	−1.5	−1.8	−2.1
Glycoprotein 49A	Mm.196617			−2.6
Glycoprotein 49B	Mm.34408	−3.2	−4.0	−2.2
LIM only 2	Mm.29266		−2.9	−3.2
Schlafen 4	Mm.38192	−1.6	−5.1	−2.4
Cell surface glycoprotein EMR 1 precursor	Mm.258979	−2.5	−3.1	−3.5
Peroxiredoxin 4	Mm.247542			−1.9
Peroxiredoxin 5	Mm.279782			−2.1
Pleckstrin	Mm.98232		−6.6	−2.3

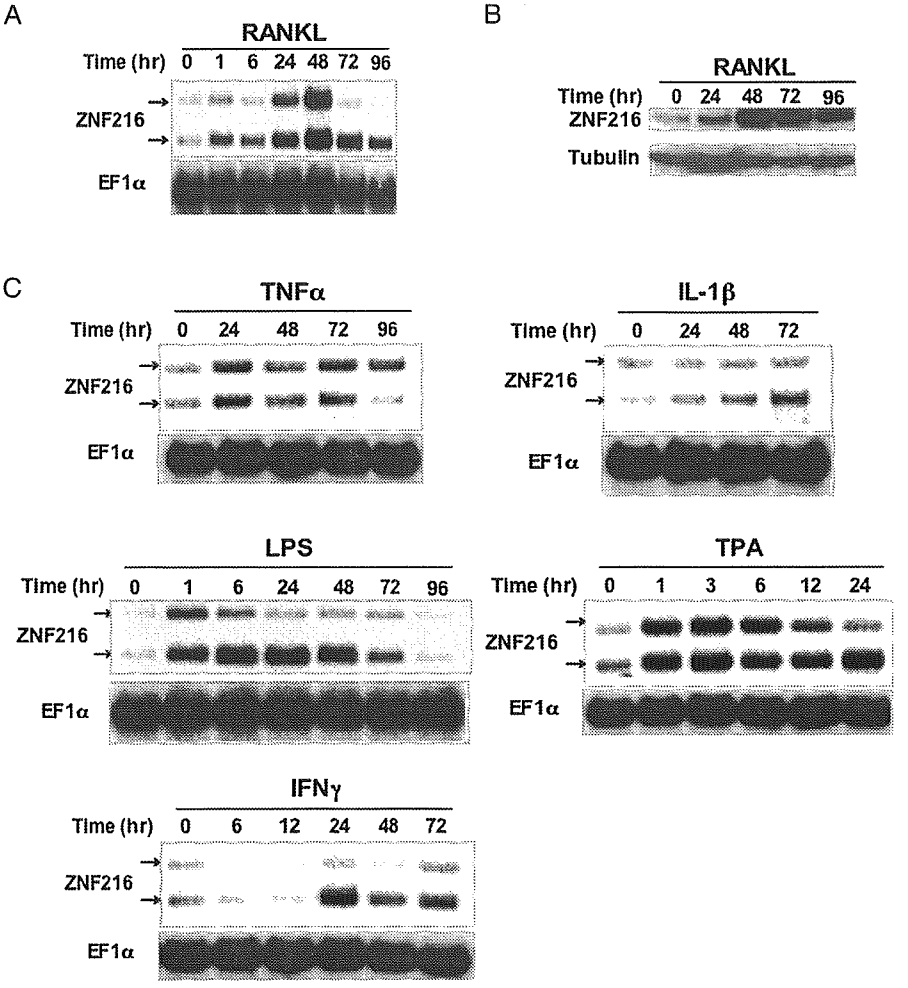

Figure 1: Expression of ZNF216. (A) The expression of ZNF216 is induced by RANKL. RAW264.7 cells were treated with RANKL (10 ng/mL) for the indicated time, and purified RNA was subjected to Northern blot analysis. The same membranes were reprobed for EF1α (elongation factor 1α) to control for loading. (B) Immunoblot analysis. The induction of ZNF216 protein is shown throughout a 96-hr time-course. The membrane was reprobed with tubulin antibody to control for protein loading. (C) Other proinflammatory cytokines or stimulators also induced ZNF216. Total RNA was prepared at the indicated time and probed for ZNF216 mRNA expression. The membrane was reprobed for EF1α as described above to control for loading.

pattern of the protein was well concordant with that of the RNA, the peak level of ZNF216 protein persisted long after 72 hr, when the RNA level had subsequently declined. RANKL-induced expression of ZNF216 was also observed in primary cultures of bone marrow macrophages (data not shown).

To examine whether expression of ZNF216 could be induced by other TNF superfamily cytokines, RAW264.7 cells were treated with TNFα. As expected,

TNFα up-regulated ZNF216, although not as much as RANKL (Fig. 1C). Both RANKL and TNFα activate a common signaling pathway through NF-κB and JNK with TNFR-associated factor (TRAF) family members (24). This intracellular pathway is known to be partially shared by those of IL-1β and LPS. As shown in Figure 1C, the expression of ZNF216 was also increased by treatment with both IL-1β and LPS. It is of interest that the expression was rapidly induced by LPS within 1 hr (Fig. 1C). In contrast, ZNF216 expression induced by IL-1β was rather weak. Thus, we hypothesized that activators of NF-κB or AP-1 might also induce ZNF216 expression. TPA, a potent activator of protein kinase C (PKC), activates NF-κB and AP-1 in rat 3Y1 fibroblasts and in the human gastric cancer cell line, MGC80-3 (25–27). As shown in Figure 1C, expression of ZNF216 was strongly induced by TPA in RAW264.7 cells. In addition, the antiviral cytokine, IFNγ, which is not known as an activator of NF-κB or AP-1, also up-regulated the expression of ZNF216 (Fig. 1C).

Ectopic Expression of ZNF216 in Osteoclast Differentiation

The ZNF216 protein is composed of 213 amino acid and contains both A20-like and AN1-like zinc finger domains (Fig. 2A). The A20-like zinc finger domain is a C2/C2 type zinc finger localized between amino acids 11–35 at the N-terminus (Fig. 2A). The AN1-like zinc finger domain is localized at amino acids 154–193 and contains the sequence CX2CX(9–12)CX(1–2)CX4CX2HX5HXC, which is similar to that of AN1, a ubiquitin-like protein in Xenopus laevis (28). To clarify the molecular function of ZNF216 in osteoclast differentiation, we generated RAW264.7 cells stably expressing either full-length or truncated forms of ZNF216, and in vitro osteoclastogenesis assays were performed. Comparable expression of ZNF216 and its mutants were confirmed by immunoblot analyses (Fig. 2A, right panel). Proliferation was not significantly affected by ectopic expression of ZNF216 mutants (not shown). Stably transfected RAW264.7 cells were seeded in 96-well plates and stimulated with RANKL for 48 hr. It is surprising that ectopic expression of full-length ZNF216 significantly suppressed TRAP-positive cell number compared with mock-infected RAW264.7 cells (Figs. 2B and C). By contrast, RAW cells expressing deletion mutations in either zinc finger domain (ΔN or ΔC) exhibited accelerated osteoclast differentiation monitored by TRAP (Figs. 2B and C). In particular, the C-terminal zinc finger domain truncated mutant (ΔC) dramatically promoted the expression of TRAP. Most of RAW264.7 cells expressing ΔC mutant were positive for TRAP, whereas mock-infected cells were only 25% TRAP positive (Figs. 2B and C). Ectopic expression of truncated mutants in RAW264.7 cells did not possess any TRAP activity without RANKL treatment, indicating that RANKL was required for the observed effects of on osteoclast differentiation (data not shown).

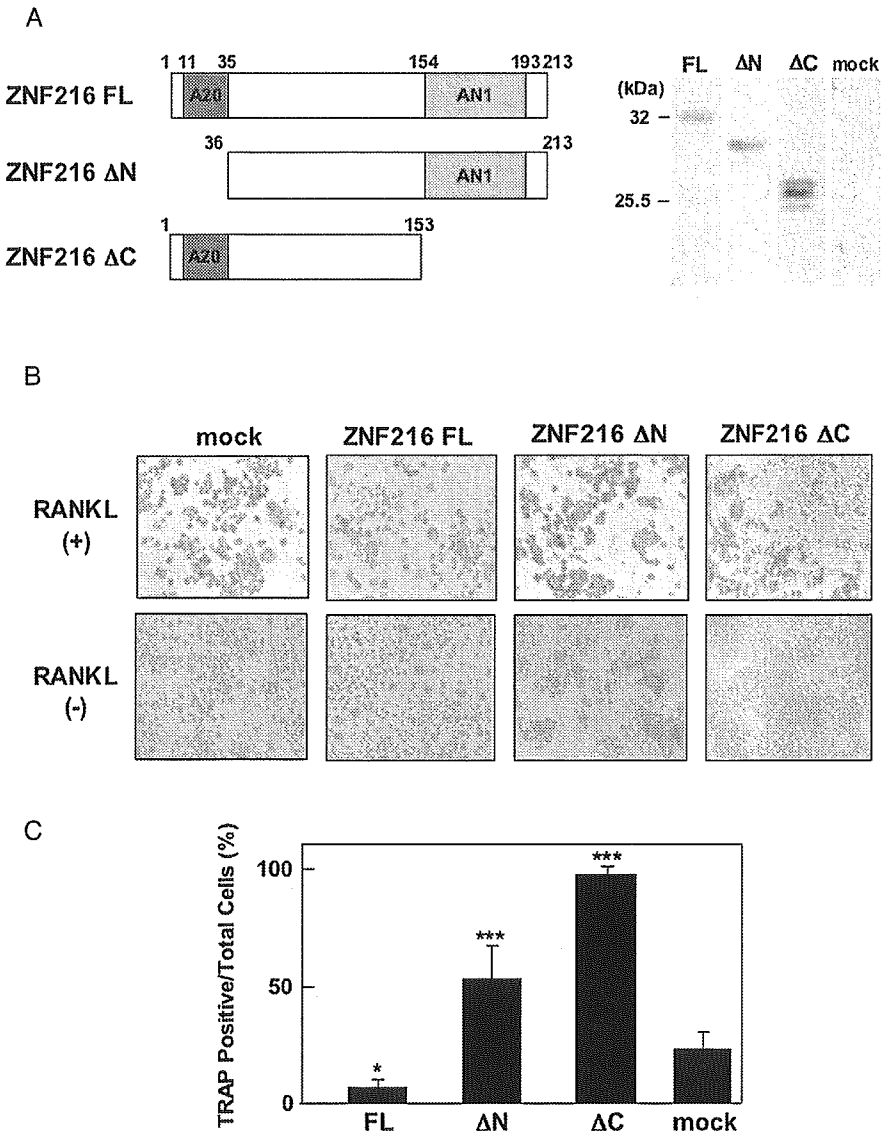

Figure 2: ZNF216 inhibits osteoclastogenesis. (A) Schematic presentation of ZNF216 and its deletion mutants (left panel). Full-length ZNF216 (213 amino acids) is denoted as ZNF216-FL. A20-like (*dark gray box*) or AN1-like (*gray box*) zinc finger domains were deleted in ZNF216-ΔN or ZNF216-ΔC, respectively. The number represents the positions of the deleted amino acid residues. Expression of ZNF216 and its mutants in RAW264.7 cells (right panel). The expression levels of the proteins in stable transfectants were comparable. ZNF216 proteins were detected by immunoblotting with anti-FLAG antibody. (B) Ectopic expression of ZNF216 inhibits RANKL-mediated osteoclastogenesis in RAW264.7 cells. Three individual RAW264.7 cell clones stably expressing full-length or truncated forms of the zinc finger domains were seeded and treated with (upper panels) or without (lower panels) RANKL (10 ng/mL). After 48 hr, cells were fixed and TRAP activity was determined. No TRAP-positive cells were observed in all cell lines without RANKL treatment. (C) The number of TRAP-positive (purple) cells, in (B), were quantified. Results represent the average values from the three clones. $^{*}P < 0.05$ vs. mock-infected cells; $^{***}P < 0.005$ vs. mock-infected cells.